X-ray Nanoscale Profiling of Layer-by-Layer Assembled Metal/Organophosphonate Films

Joseph A. Libera,[†] Richard W. Gurney,[‡] SonBinh T. Nguyen,[‡] Joseph T. Hupp,[‡] Chian Liu,[§] Ray Conley,[§] and Michael J. Bedzyk*,[†]

Department of Materials Science and Engineering, Department of Chemistry, and Nanoscale Science and Engineering Center, Northwestern University, Evanston, Illinois 60208, and Advanced Photon Source, Argonne National Laboratory, Argonne, Illinois 60439

Received May 3, 2004. In Final Form: July 7, 2004

The nanoscale structure of multilayer metal/phosphonate thin films prepared via a layer-by-layer assembly process was studied using specular X-ray reflectivity (XRR), X-ray fluorescence (XRF), and long-period X-ray standing wave (XSW) analysis. After the SiO_2 X-ray mirror surfaces were functionalized with a monolayer film terminated with phosphonate groups, the organic multilayer films were assembled by alternating immersions in (a) aqueous solutions containing Zr^{4+}, Hf^{4+}, or Y^{3+} cations and then (b) organic solvent solutions of PO_3-R-PO_3, where R was a porphyrin or porphyrin-square spacer molecule. The different heavy metal cations provided X-ray fluorescence marker layers at different heights within the different multilayer assemblies. The XSW measurements used a 22 nm period Si/Mo multilayer mirror. The long-period XSW generated by the zeroth-order (total external reflection) through fourth-order Bragg diffraction conditions made it possible to examine the Fourier transforms of the fluorescent atom distributions over a much larger q_z range in reciprocal space than previously achieved.

Introduction

Thin films based on mono- and multilayer metal/organophosphonate chemistry continue to receive developmental effort primarily by modification of the molecular structure of the organophosphonate component.[1,2] Multifunctional, microporous thin films with uniform thicknesses and a well-defined porous structure are desirable from a functionalized nanomaterials perspective. We have had a particular interest in molecule-derived versions of these materials. Thin films of this kind can function as molecular sieves,[3−5] frameworks for size-selective heterogeneous catalysis,[6] chemical sensors,[7,8] and sensitizing dye layers in liquid-junction solar cells.[9−11] Pillared organic films containing nanoscopic pores can be formed by cross-linking zirconium phosphate-like layers with several types of diphosphonic acids.[12,13] The work by Katz and co-workers specifically on diphosphonic acid porphyrin incorporation should be noted.[14,15]

A major challenge in the design of functional thin-film materials is the elucidation of their structure and quality. This is particularly true in the formation of metal/phosphonate multilayer assemblies where the organophosphate spacer molecules have large asymmetric forms. Early work in this field showed that high-quality multilayers could be made by using simple linear molecules such as 1,10-decanediylbis(phosphonate) and (11-hydroxyundecyl)phosphonic acid.[16,17] Linear fits of the ellipsometric thicknesses with the number of layers were observed. Other notable examples of ordered-film characterization include X-ray powder diffraction studies of layer spacing,[18] as well as angle-resolved XPS studies of films featuring sequential Hf/Zr/Y layering.[19] More recent work has incorporated oligothiophene chromophores.[20]

In our present study, we use long-period X-ray standing waves (XSWs) generated by total external reflection (TER)[21,22] and Bragg diffraction from a layered synthetic microstructure (LSM)[23,24] to examine the heavy-atom profiles $\rho(z)$ within the multilayer metal/phosphonate thin

* To whom correspondence should be addressed. Phone: (847) 491-3570. Fax: (847) 467-2269. E-mail: bedzyk@northwestern.edu.
[†] Department of Materials Science and Engineering and Nanoscale Science and Engineering Center, Northwestern University.
[‡] Department of Chemistry and Nanoscale Science and Engineering Center, Northwestern University.
[§] Argonne National Laboratory.

(1) Bakiamoh, S. B.; Blanchard, G. J. *Langmuir* **2002**, *18*, 6246−6253.
(2) Zwahlen, M.; Tosatti, S.; Textor, M.; Hahner, G. *Langmuir* **2002**, *18*, 3957−3962.
(3) Williams, M. E.; Hupp, J. T. *J. Phys. Chem. B* **2001**, *105*, 8944−8950.
(4) Czaplewski, K. F.; Hupp, J. T.; Snurr, R. Q. *Adv. Mater.* **2001**, *13*, 1895−1897.
(5) Zhang, J. L.; Williams, M. E.; Keefe, M. H.; Morris, G. A.; Nguyen, S. T.; Hupp, J. T. *Electrochem. Solid State Lett.* **2002**, *5*, E25−E28.
(6) Hu, A.; Ngo, H. L.; Lin, W. B. *Angew. Chem., Int. Ed.* **2003**, *42*, 6000−6003.
(7) Mines, G. A.; Tzeng, B. C.; Stevenson, K. J.; Li, J. L.; Hupp, J. T. *Angew. Chem., Int. Ed.* **2002**, *41*, 154−157.
(8) Sun, S. S.; Lees, A. J. *J. Am. Chem. Soc.* **2000**, *122*, 8956−8985.
(9) Splan, K. E.; Massari, A. M.; Hupp, J. T. *J. Phys. Chem* **2004**, *in press*.
(10) Kaschak, D. M.; Lean, J. T.; Waraksa, C. C.; Saupe, G. B.; Usami, H.; Mallouk, T. E. *J. Am. Chem. Soc.* **1989**, *121*, 3435−3445.
(11) Abdelrazzaq, F. B., Kwong, R. C.; Thompson, M. E. *J. Am. Chem. Soc.* **2002**, *124*, 4796−4803.
(12) Clearfield, A.; Wang, Z. K. *J. Chem. Soc., Dalton Trans.* **2002**, 2937−2947.
(13) Mallouk, T. E. *Acc. Chem. Res.* **1998**, *31*, 209−217.
(14) Ungashe, S. B.; Wilson, W. L.; Katz, H. E.; Scheller, G. R.; Putvinski, T. M. *J. Am. Chem. Soc.* **1992**, *114*, 8717−8719.
(15) Katz, H. E. *Chem. Mater.* **1994**, *6*, 2227−2232.
(16) Lee, H.; Kepley, L. J.; Hong, H. G.; Akhter, S.; Mallouk, T. E. *J. Phys. Chem.* **1988**, *92*, 2597−2601.
(17) Putvinski, T. M.; Schilling, M. L.; Katz, H. E.; Chidsey, C. E. D.; Mujsce, A. M.; Emerson, A. B. *Langmuir* **1990**, *6*, 1567−1571.
(18) Hong, H.-G.; Sackett, D. D.; Mallouk, T. E. *Chem. Mater.* **1989**, *3*, 521−527.
(19) Akhter, S.; Lee, H.; Hong, H.-G.; Mallouk, T. E. *J. Vac. Sci. Technol., A* **1989**, *7*, 1608−1613.
(20) Horne, J. C.; Blanchard, G. J. *J. Am. Chem. Soc.* **1998**, *120*, 6336−6344.
(21) Bedzyk, M. J.; Bommarito, G. M.; Schildkraut, J. S. *Phys. Rev. Lett.* **1989**, *62*, 1376−1379.
(22) Wang, J.; Bedzyk, M. J.; Penner, T. L.; Caffrey, M. *Nature* **1991**, *354*, 377−380.
(23) Bedzyk, M. J.; Bilderback, D.; White, J.; Abruna, H. D.; Bommarito, M. G. *J. Phys. Chem.* **1986**, *90*, 4926−4928.

10.1021/la048904b CCC: $27.50
Published on Web 08/19/2004

films prepared via a layer-by-layer assembly process on the SiO_2 surface of the LSM. Within each film, we selectively generate an XSW with a period ranging from 200 to 4 nm by scanning in incident angle θ through the zeroth-order (TER) to fourth-order Bragg diffraction conditions from an underlying Si/Mo LSM which has a 21.6 nm d spacing. Quantitative structural information is derived by comparing the angle θ dependence of the measured heavy-atom fluorescence yield modulations to a yield predicted by dynamical X-ray scattering theory for a model $\rho(z)$.

In addition to measuring the individual heavy atom $\rho(z)$ profiles with XSW, we also measured the coverage (effective area density) of each heavy element by X-ray fluorescence (XRF). We also measured the overall electron density profile of the films with specular X-ray reflectivity (XRR) performed on a series of related thin-film samples that were deposited on plain Si substrates with a SiO_2 surface layer, but without the intervening LSM.

Experimental Section

Substrate Fabrication. The metal/organophosphonate films were grown on SiO_x surfaces. The SiO_x surfaces were atop Si(001) substrates or atop the final sputter-deposited Si layer of Si/Mo LSM mirrors that were deposited on Si(001) substrates (37.5 mm long by 12.5 mm wide by 2.5 mm thick). The surface roughness of these prepolished Si(001) wafers was 2−5 Å rms. The Si/Mo LSMs were prepared as a single batch in the X-ray optics fabrication facilities at the Advanced Photon Source using dc magnetron sputtering at an Ar pressure of 2.3 mTorr. Each LSM had $N = 15$ Si/Mo bilayers deposited. The XRR analysis of these LSMs, which will be described below, determined that the bilayer thickness (period) was $d = 21.6$ nm and the Si:Mo thickness ratio was 4.49. The terminating surface of the LSM was the final Si layer. The actual thickness of this top Si layer was slightly larger than the other Si layers due to the SiO_x native oxide growth.

Film Preparation. All substrates in this study received an identical primer monolayer prior to layer deposition. The primer chemistry was based on the work of Horne et al.,[20] with slight modifications. In the first step, the substrates were placed in piranha solution (2:1 sulfuric acid/hydrogen peroxide) to remove organic contaminants from the surface, then rinsed with ultrapure Millipore water, and dried under a stream of N_2. (*Caution! This solution can react violently with organics.*)

Immediately afterward the substrates were immersed in 2 M HCl for 5 min, rinsed with ultrapure water, dried under a stream of dry N_2, and oven-dried at 80 °C for 15 min. The substrates were placed in an 80 °C solution of anhydrous octanol and (3-aminopropyl)trimethoxysilane (APTMS) (100:1 v/v) for 10 min, followed by rinsing with hexanes and ultrapure water, drying under a stream of dry N_2, and drying in an oven at 80 °C for 30 min. Phosphorylation was followed by placing the substrates into a mixture of 0.1 M $POCl_3$ and 0.1 M 2,4,6-collidine in anhydrous acetonitrile (ACN) for 1 h. The samples were then heated in warm, dry ACN for 15 min, followed by rinses with ACN and ultrapure water. The samples were then dried under a stream of dry N_2, placed in an aqueous solution of 5 mM $ZrOCl_2 \cdot 8H_2O$ for 2 h, rinsed with ultrapure water, and dried under a stream of dry N_2. The preparation of the molecular overlayers for the samples of this study is shown schematically in Figure 1. Samples C2, C4, C8, and D8 were prepared on primed blank Si(001) substrates (no LSM) and were used for XRR studies. Samples A1 and A8 were prepared on LSM substrates and were used for XSW studies. Details of the molecular structure for sample A8 are also shown in Figure 1, and the molecular structure of the porphyrin square used for samples A1 and D8 is given in Figure 2. While samples A1 and D8 were indeed prepared as indicated in Figure 1, it is important to note that there are four diphosphonic acid porphyrin constituents for each porphyrin-square macromolecule. In Figure 1 each circle, rectangle, or square represents the material added in a single immersion step into an appropriate solution as described in the following: (1) porphyrin, 1 mM solution of diphosphonic acid porphyrin in dimethyl sulfoxide (DMSO) for 2 h; (2) porphyrin square, 0.0125 mM solution of porphyrin square in DMSO for 2 h; (3) Zr, 5 mM $ZrOCl_2 \cdot 8\,H_2O$ for 30 min; (4) Hf, 5 mM $HfOCl_2 \cdot 8\,H_2O$ for 30 min; (5) Y, 5 mM aqueous solution of $Y(NO_3)_3$ for 30 min. Full details of the synthesis and characterization of the porphyrin and porphyrin-square molecule are given elsewhere.[25]

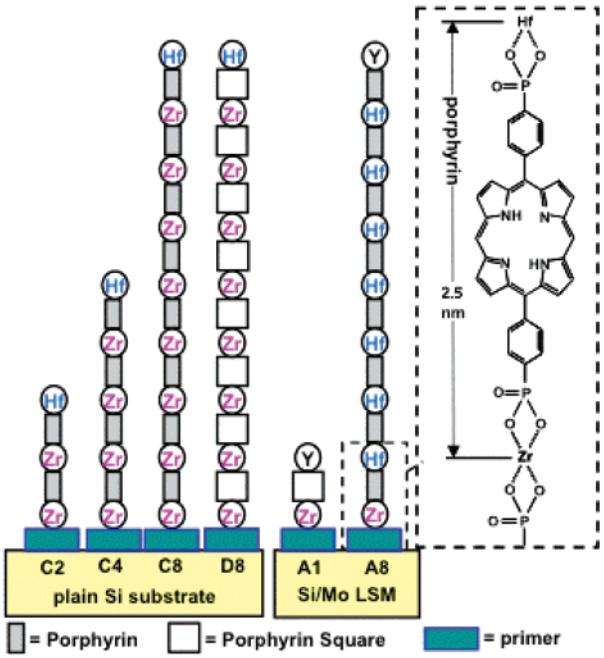

Figure 1. Schematic diagram of the layered films used in this study. Circles indicate material added by immersion of the samples into aqueous solutions of the indicated atom. The gray shaded rectangle indicates material added by immersion into a solution of diphosphonic acid porphyrin in DMSO. An open square indicates material added by immersion into a solution of porphyrin square in DMSO. The expanded molecular diagram (on the right-hand side) shows the details for sample A8 including the primer, diphosphonic acid porphyrin, and first Hf layer. The metal−phosphonate linkage is more complex (but probably no longer) than sketched (see the text).

X-ray Standing Waves. Long-period XSW analysis is generally used for measuring element-specific atomic distribution profiles $\rho(z)$ in a surface overlayer structure. In our present case, the XSW is generated by TER[21,22,26] and Bragg diffraction from a periodic LSM.[23,24] The XSW, which is produced by the interference between the incident and reflected X-ray plane waves, has planes of equal intensity (nodes and antinodes) that are parallel to the LSM interfaces. (We will choose the z direction to be perpendicular to this set of parallel interfaces.) In the vacuum (or air) region above the reflecting surface, the XSW period is $D = \lambda/(2 \sin \theta) = 2\pi/q$. Even though the X-ray wavelength, λ, is on the order of angstroms, the XSW period can be very much longer (varying with the incident angle, θ, from a couple of micrometers to a couple of nanometers). This is due to TER and Bragg diffraction from an LSM occurring at very small incident angles, θ, or more generally at small values of the scattering vector, q. The phase (v) of the XSW shifts inward by 180° as the incident angle (θ) is scanned through the region of TER or across a Bragg reflection. This induces a modulation in the X-ray fluorescence yield from a given atom that is characteristic of the spatial distribution profile $\rho(z)$ for that atomic species.

The measured atomic fluorescence yield $Y(\theta)$ at any incident angle θ is the integral of the product of the unknown atomic

(24) Bedzyk, M. J.; Bilderback, D. H.; Bommarito, G. M.; Caffrey, M.; Schildkraut, J. S. *Science* **1988**, *241*, 1788−1791.

(25) Massari, A. M.; Gurney, R. W.; Schwartz, C. P.; Nguyen, S. T.; Hupp, J. T. *Langmuir*, in press.

(26) Bedzyk, M. J.; Bommarito, G. M.; Caffrey, M.; Penner, T. L. *Science* **1990**, *248*, 52−56.

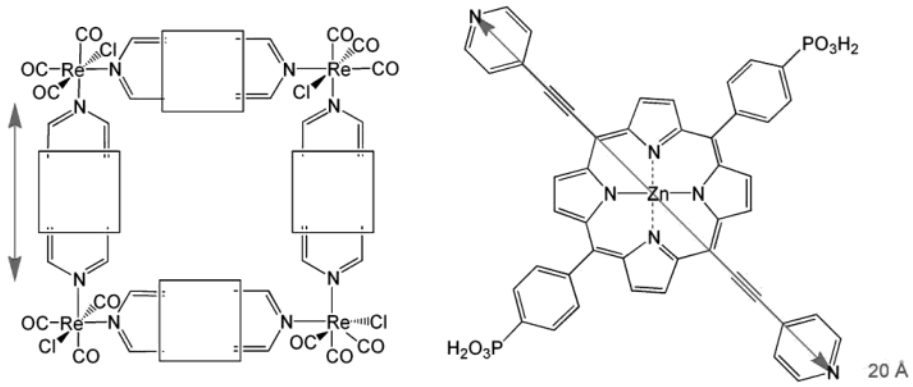

Figure 2. Molecular diagram of the porphyrin-square macromolecule used in samples A1 and D8. The Re atoms form a plane which is expected to lie parallel to the sample surface. The four porphyrin constituents (phosphonic acid version shown) are expected to assemble in the films with the PO_3-PO_3 axes oriented roughly perpendicular to the plane of the Re atoms and thus perpendicular to the sample surface.

density profile $\rho(z)$ with the calculated **E** field intensity $I(\theta,z)$. For cases in which the sample films are very thin (e.g., less than 1 nm) and of much lower density than the substrate, the film will only have a small effect on the **E** field intensity within the film. This is especially true for angles greater than the critical angle of the film. However, in this study we include samples with an overall film thickness of ~19 nm which have a strong effect on the **E** field intensity in the film at very small angles. In particular, we observe a resonant cavity phenomenon,[27] which produces a strong enhancement of the fluorescence in the film's TER region.

In previous long-period XSW studies using LSMs,[24,28] the LSM period was typically in the range of 2.5−8 nm and the XSW analysis only made use of the zeroth-order (TER) and first-order Bragg peaks. The higher order Bragg peaks were typically too weak (R_{peak} < 15%) to generate an XSW with sufficient fringe visibility. In this study, we use for the first time an LSM with a much larger d spacing to produce a variable-period XSW over several orders of Bragg diffraction peaks. Figure 3a shows the measured and calculated X-ray reflectivity from the LSM substrates used in this study. Figure 3a also lists the XSW standing wave period (D) in the vacuum at each Bragg peak position. (Note that at very small incident angles refraction causes an upward shift of the external Bragg angle and also causes the XSW period outside the LSM to be significantly smaller than the period (d_m) inside the LSM.) This ability to generate a variable-period XSW over a large range from 5 to 30 nm allows us to measure atomic distributions over these same length scales. In essence, the measured modulations in the fluorescence yield from an overlayer atom lead to a measure of the Fourier transform $F(q)$ of the distribution $\rho(z)$ of that atom.

XSW measurements were performed at the National Synchrotron Light Source (NSLS) X15A beamline using $E_\gamma = 18.3$ keV ($\lambda = 0.677$ Å) incident X-rays to excite Zr K, Y K, Zn K, Re L, and Hf L X-ray fluorescence. The incident beam was conditioned by a double-crystal Ge(111) monochromator followed by a 0.02 mm high by 2 mm wide slit. The reflectivity and fluorescence data were simultaneously collected in a $\theta-2\theta$ scan covering the range of TER through the first four Bragg peaks of the LSM mirror. Multichannel-analyzer (MCA) X-ray fluorescence spectra were collected at each angle step of the scan using an energy-dispersive Si(Li) solid-state detector. A random pulse generator of constant average input pulse frequency was used for dead-time correction. A sin θ geometrical X-ray beam footprint correction was applied to the fluorescence data. Finally, the fluorescence yields were normalized to unity at an angular position where the reflectivity was zero.

X-ray Reflectivity. XRR was performed at the Northwestern University X-ray Facility using Cu Kα (8.04 keV) X-rays from a rotating anode vertical line source coupled to an Osmic parabolic, graded d spacing, collimating, multilayer mirror, followed by a two-circle diffractometer with vertical axes. The beam size was 0.10 mm wide by 10 mm high. The instrumental resolution was $\Delta q = 5 \times 10^{-3}$ Å^{-1}. The XRR data from the NaI detector were dead-time corrected and background subtracted.

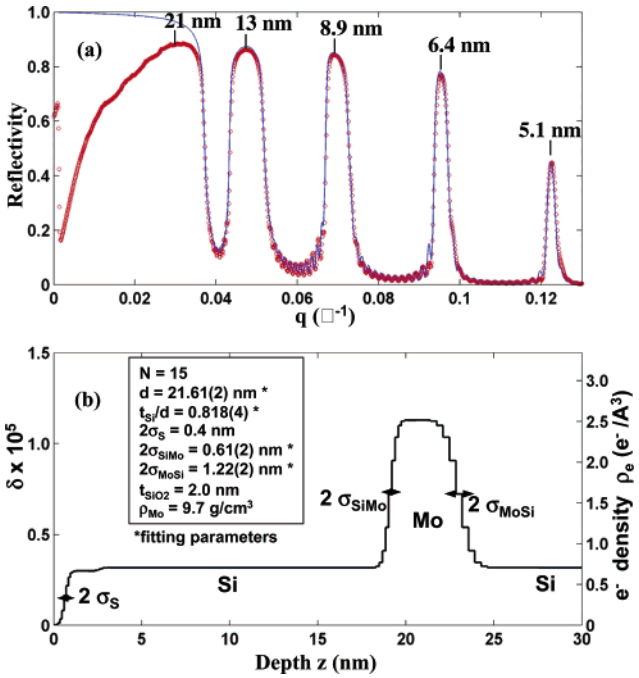

Figure 3. (a) Measured X-ray reflectivity data (open circles) from the clean LSM substrate along with a dynamical theory fit to the data (solid line) over a range that includes the zeroth (TER) through fourth Bragg peaks. The XSW period in the air above the LSM is $D = 2\pi/q$. This is listed at the center of each Bragg peak just above the peak. (b) Profile of the electron density model (also shown as the index of refraction parameter, δ) determined from the fit in (a). Only the topmost Si/Mo bilayer is shown.

X-ray Fluorescence Coverage Measurement. The absolute coverage of each of the heavy atoms within each film was measured by an XRF comparison to a Sr-implanted standard that had an effective coverage of 10.0 nm^{-2} that was calibrated by Rutherford backscattering (RBS). MCA spectra were collected from the standard and all samples using identical incident beam and fluorescence detector collection geometry. At $E_\gamma = 18.3$ keV the atomic X-ray fluorescence sensitivity factors[29] for Zn Kα, Y Kα, Zr Kα, Hf Lα, and Re Lα relative to Sr Kα are 0.330, 1.11, 1.23, 0.352, and 0.497, respectively.

(27) Wang, J.; Bedzyk, M. J.; Caffrey, M. *Science* **1992**, *258*, 775−778.
(28) Barbee, T. W.; Warburton, W. K. *Mater. Lett.* **1984**, *3*, 17−23.
(29) Puri, S.; Chand, B.; Mehta, D.; Garg, M. L.; Singh, N.; Trehan, P. N. *At. Data Nucl. Data Tables* **1995**, *61*, 289−311.

Table 1. Results from XRR and XRF Analysis for All Samples[a]

sample	N	ρ_F/ρ_{Si}	$t_{F,e}$, nm	t_F, nm	σ_{FS}, nm	σ_{VF}, nm	Θ_{Zr}, nm^{-2}	Θ_{Hf}, nm^{-2}	Θ_Y, nm^{-2}	$\Theta_{Zn} = \Theta_{Re}$, nm^{-2}
C2	2	0.38(2)	5.5	4.2(1)	0.45(5)	0.8(3)	4.3(2)	3.1(2)		
C4	4	0.50(2)	10.5	8.5(1)	0.25(5)	1.4(3)	9.9(5)	9.8(5)		
C8	8	0.58(2)	20.5	18.6(1)	0.25(5)	1.6(3)	24.6(9)	3.3(2)		
D8	8	0.60(2)	20.5	13.1(1)	0.20(5)	1.3(3)	13.3(7)	3.1(2)		2.6(3)
A1	1	n/a	3.0	n/a	n/a	n/a	1.32(7)		0.50(3)	0.05(2)
A8	8	n/a	20.5	19.0(2)	n/a	n/a	1.07(7)	17.7(9)	14.0(8)	

[a] See Figure 1. The electron density of the film relative to the Si substrate, ρ_F/ρ_{Si}, the film thickness, t_F, and the Gaussian widths of the film−substrate Interface, σ_{FS}, and film−air interface, σ_{VF}, were measured by XRR. The expected film thickness, $t_{F,E}$, is based on a 2.5 nm metal atom-to-metal atom spacing plus 0.5 nm for the primer layer. The measured depth-integrated atomic coverages, Θ_{Zr}, Θ_{Hf}, Θ_Y, Θ_{Zn}, and Θ_{Re}, were determined by XRF.

Results and Discussion

Si/Mo LSM Substrate Modeling. Before accurately determining the overlayer structure with the long-period XSW method, we need to first accurately model the complex index of refraction profile for the sample substrate. Therefore, reflectivity measurements of a blank (no overlayer) LSM substrate were taken. Reflectivity was taken at 12.4 keV and is shown in Figure 3a. Since this study is the first to use large-*d*-spacing LSM mirrors for generating an XSW, considerable attention was focused on developing reliable reflectivity modeling techniques. Essential guidance was obtained from earlier work[30,31] regarding the asymmetric nature of the Si/Mo versus Mo/Si interfaces. In Figure 3b we show the model for the electron density profile (and corresponding refraction parameter δ) that gives the best fit to the XRR data shown in Figure 3a.

The theoretical or simulated reflectivity (Figure 3a) for the LSM was calculated by applying Parratt's recursion formulation to the model.[32] To calculate the XSW intensity $I(\theta,z)$, this same dynamical scattering theory was then extended to allow computation of the **E** field at any point within the model structure.[33,34] The model consists of a series of parallel layers (slabs). Each layer has a constant index of refraction ($n_j = 1 - \delta_j - i\beta_j$), thickness ($t_j$), and interfacial width (σ_j). The simplest application in the case of the LSM substrate is to use a single layer in the model for each Si and Mo sublayer. The procedure also allows for the use of a Debye−Waller factor approach for simulating the interface roughness effect on the reflectivity. Using this approach, we could not obtain satisfactory fits to the observed reflectivity, especially at the lower order Bragg reflections. Good fits were obtained only when the projected electron density profile of each interface was modeled using a graded-interface model.[35] This more accurately calculates how the interface affects the phases, as well as the amplitudes, of transmitted and reflected **E** fields. The interfaces between Si/Mo and Mo/Si were separately modeled using an error function profile approximated by 10 layers in the LSM model. The width, σ_{SiMo}, of the Si on Mo interface was fixed at half the width, σ_{MoSi}, for the Mo on Si interface, consistent with previous reports[30,31] on the structure of Si/Mo films. As a further model refinement, the Si/Mo layer-pair thickness (*d* spacing) of the $N = 15$ layer pairs was allowed to change as a linear function of the depth *z*. From this, we found a 2% reduction of the *d* spacing over the entire LSM thickness due to a gradual reduction in the sputter deposition rate.

The graded *d* spacing refinement to the model results in considerable improvement in matching observed peak asymmetries. The solid line in Figure 3a shows the final simulated reflectivity, which has an excellent match to the measured data. (The low-angle mismatch is due to the incident X-ray beam over-subtending the length of the sample.) We can now use this XRR-determined model for the LSM as a known quantity that will be used to accurately describe the **E** field intensity within the overlayer film, which in turn will be used to simulate the observed heavy-atom X-ray fluorescence yields.

Initial XRF Characterization of the Primer Layer and Porphyrin Square. All samples were prepared using an identical substrate-priming procedure, leaving a PO_3-functionalized substrate surface terminated with zirconium ions. Due to a comparatively weak P Kα X-ray fluorescence signal, the XRF for this particular setup was not able to directly measure the coverage of P. Samples A1 and A8 of this study, as well as two others not listed in this report, contained Zr only in the primer layer (Figure 1). XRF-measured coverages for these four samples were in the range of 1.0−1.6 Zr atoms/nm^2. (See Table 1 for a list of XRF-measured heavy-atom coverages.) For sample D8 with $N = 8$ layers, we can convert the Re (or Zn) measured atomic coverage of 2.6 Re atoms/nm^2 into 0.33 Re atom/nm^2 per layer, which corresponds to a macromolecular footprint of 12 nm^2. (Here we assume 4 Re (or 4 Zn) atoms per macromolecular square as shown in Figure 2.) This footprint would correspond to a 3.5 × 3.5 nm^2 square, which is a reasonable random packing density, given an approximate length of 3.2 nm for the OC−Re−porph−Re−CO shown in Figure 2. The XRF finding that the single porphyrin-square layer of sample A1 has 15% of the expected Re (or Zn) coverage will be corroborated in the XSW section, where this single layer appears to be vertically collapsed. The complexation, at the end groups of the diphosphonic acid porphyrin molecule in Figures 1 and 2 (right-hand side), is shown schematically as one metal ion per PO_3/PO_3 junction. This is based solely on charge balance (at least for zirconium(IV) and hafnium(IV)). If metal ions retain charged halo, oxo, or hydroxo ligands, however, the metal:phosphonate ratio would likely be higher. In layered Zr/phosphonate compounds featuring sterically undemanding alkane spacers, continuous 2-D Zr/phosphonate layers, rather than discrete junctions, are formed.[36] In these layers, each oxygen atom of a given phosphonate binds to a different zirconium ion; i.e., the chelation motif simplistically sketched in Figure

(30) Petfordlong, A. K.; Stearns, M. B.; Chang, C. H.; Nutt, S. R.; Stearns, D. G.; Ceglio, N. M.; Hawryluk, A. M. *J. Appl. Phys.* **1987**, *61*, 1422−1428.
(31) Slaughter, J. M.; Schulze, D. W.; Hills, C. R.; Mirone, A.; Stalio, R.; Watts, R. N.; Tarrio, C.; Lucatorto, T. B.; Krumrey, M.; Mueller, P.; Falco, C. M. *J. Appl. Phys.* **1994**, *76*, 2144−2156.
(32) Paratt, L. G. *Phys. Rev.* **1954**, *95*, 359−369.
(33) Bommarito, G. M. InSitu Studies of Electrochemical Interfaces Using X-Ray Standing Waves. Ph.D. Thesis, Cornell University, 1992.
(34) Ghose, S. K.; Dev, B. N. *Phys. Rev. B* **2001**, *63*, 245409-1-11.
(35) Nevot, L.; Croce, P. *Rev. Phys. Appl.* **1980**, *15*, 761.
(36) Cao, G.; Hong, H. G.; Mallouk, T. E. *Acc. Chem. Res.* **1992**, *25*, 420−427.

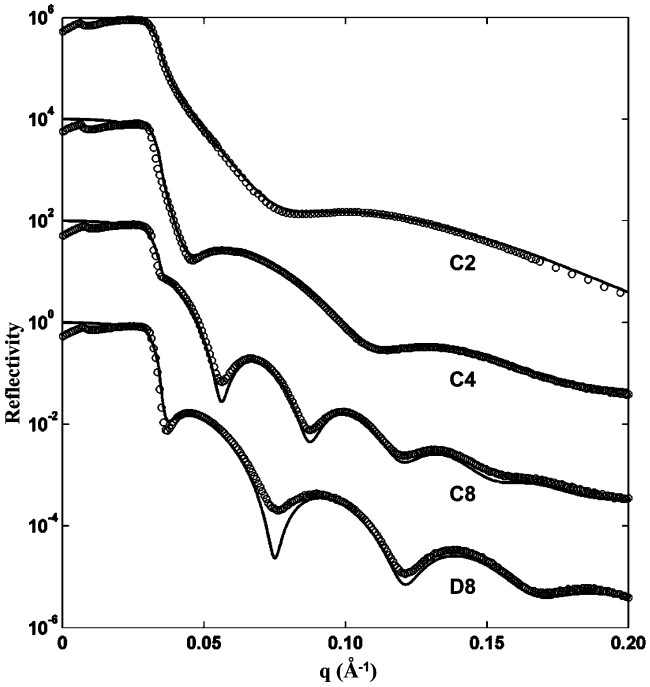

Figure 4. X-ray reflectivity data (open circles) for samples C2, C4, C8, and D8. (See Figure 1.) The theoretical fits (solid lines) correspond to a single-slab model with graded interfaces with the fit parameters listed in Table 1.

1 is absent. If chelation is likewise unused here, and if Zr ions retain an oxo ligand, an alternative stoichiometry, more closely structurally resembling the known 2-D layers, would be two zirconium ions per PO_3/PO_3 junction.

Solely on the basis of this expected complexation (two metal ions per junction) and the molecular footprint, the Zr, Hf, or Y atomic coverage per layer, in, for example, sample D8, should be 0.65 atom/nm^2. The measured Zr and Hf coverages per layer in sample D8 are, respectively, 2.5 and 4.8 times higher. This excess, and similar Zr, Hf, or Y excesses in the other samples, indicates that these metal ions have additional modes of incorporation in these films.

XRR and XRF Analysis. The reflectivity data for samples C2, C4, C8, and D8 and theoretical fits are shown in Figure 4 with the fit-determined parameters listed in Table 1. The same graded-interface modeling procedure, as described above, was used for fitting the observed reflectivity. The layered model consisted of a Si substrate, a 2.0 nm SiO_2 layer for the native oxide, and a single layer for the film. The free fitting parameters were the σ widths of the error function interface profile, σ_{VF} for the air/film interface, σ_{FS} for the film/native oxide interface, t_F for the film thickness, and ρ_F/ρ_{Si} for the ratio of the film to Si electron density (where $\rho_{Si} = 699$ e/nm^3). The expected film thickness ($t_{F,e}$) is based on the approximation of 0.5 nm for the primer layer plus 2.5 nm per layer based on the fully extended molecular configuration. (See Table 1.) For the $N = 2$, 4, and 8 layer porphyrin films we measure thicknesses (t_F) that are slightly less than expected (average layer thicknesses of 1.85, 2.0, and 2.26 nm, respectively, versus 2.5 nm), but agree well with an average layer thickness of 2.1 nm obtained previously by a lower precision approach (atomic force microscopy) using micropatterned films.[37] If the smaller than expected layer thicknesses are indicative solely of tilting of the phosphonate−porphyrin−phosphonate axis away from surface normality (90°), the average angles would be ca. 48°, 53°, and 66°, respectively.

XRF coverage measurements give Zr atomic densities of 4.3, 9.9, and 24.6 Zr atoms/nm^2 for samples C2, C4, and C8, respectively. Assuming coverages similar to the initial Zr surface density found for samples A1 and A8, we expected maximum Zr coverages of 3.4, 6.8, and 13.6 Zr atoms/nm^2, respectively, for samples C2, C4, and C8. This indicates that the Zr excess is increasing with each additional layer. Samples C2, C4, C8, and D8 were terminated by a Hf metal layer to evaluate the use of Hf as a metal marker atom. The observed Hf atom coverages of 3.1, 3.3, and 3.1 Hf atoms/nm^2 for samples C2, C8, and D8 are nearly triple the Zr surface densities of the films grown with a single Zr layer. The value of 9.8 Hf/nm^2 obtained for sample C4 is abnormally high and is attributed to free particles containing Hf and not associated with the film. Since XSW analysis is not possible on these non-LSM samples, the partitioning of the 9.8 nm^{-2} observed coverage into film and contaminant particle contributions was not determined.

Sample D8 was prepared to be similar to C8 but using a different organophosphonate layer. The porphyrin-square molecule used for D8 has an identical PO_3-to-PO_3 axis but is different in that four such porphyrin molecules are assembled into the square configuration (Figure 2). Nominally, we expected D8 to have the same 2.26 nm per layer thickness as C8. However, the measured average layer thickness was found to be 1.61 nm, implying a more tilted structure. Again, there is good agreement with atomic force microscopy measurements which yield 1.9 ± 0.4 nm per layer.[25]

The XRR-measured average electron densities expressed as ρ_F/ρ_{Si} for samples C2, C4, and C8 were found to be 0.38, 0.50, and 0.58, respectively. The porphyrin-square macromolecule shown in Figure 2 has $Z = 2284$ electrons and as described above for sample D8 takes up a footprint of 12 nm^2 and has a layer thickness of 1.61 nm. This corresponds to a partial electron density of 2284/12/1.6 = 119 e/nm^3. On the basis of the XRF coverage, the partial film averaged electron density for Zr is (40 × 13.3)/8/1.6 = 42 e/nm^3, and that for Hf is (72 × 3.1)/8/1.6 = 17 e/nm^3. This would lead to 178 e/nm^3 for the average electron density of the D8 film as depicted in Figure 1. The reason that this is only 42% of the XRR-measured electron density is due to unaccounted for low-Z-containing molecules, such as DMSO solvent molecules, that fill in the large open spaces of this microporous film. Since the C series of films with porphyrin molecules (Figure 1, right-hand side) did not contain a Zn (or Re), we cannot make a similar XRF deduction concerning the lateral packing of the porphyrin molecules as we just did for the porphyrin-square molecules. We can only compute a lower limit of 0.45 nm^2 for the molecular footprint for C8, by assuming there is no residue (e.g., no solvent) in the film. This is based on $Z = 342$ for the PO_3-R-PO_3 molecule, the XRR-measured $\rho = 405$ e/nm^3 and layer thickness of 2.26 nm, and the XRF-measured Zr and Hf coverages.

XSW Analysis. The XSW measurements of samples A1 and A8 were performed at 18.3 keV to provide excitation of the highest energy X-ray fluorescence line of interest, namely, Zr Kα. Prior to collection of a long-count-time XSW data set, a relatively quick reflectivity scan was taken, which is shown in Figure 5d for sample A8. The dip in the reflectivity in the TER plateau at $q = 0.032$ Å^{-1} is the only obvious deviation from a bare substrate reflectivity curve (Figure 3a) and is due to a resonant cavity (or waveguide) effect within the film.[27] Using the simplest

(37) Massari, A. M.; Gurney, R. W.; Wightman, M. D.; Huang, C. H. K.; Nguyen, S. B. T.; Hupp, J. T. *Polyhedron* **2003**, *22*, 3065−3072.

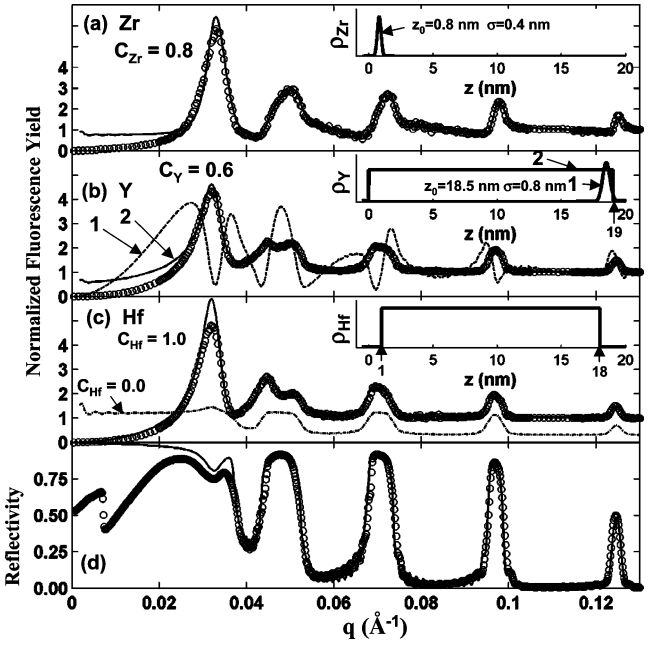

Figure 5. Sample A8 XSW results. Simultaneously measured reflectivity and Zr Kα, Y Kα, and Hf Lα X-ray fluorescence yields (open circles) and best theoretical fits (solid lines). In (c) a theoretical simulation (dashed−dotted line offset vertically for clarity) is shown for a 100% extended uniform distribution. The insets show the atom distribution $\rho(z)$ models that were used for the fluorescence yield fits shown in (a−c). As discussed in the text, the Zr and Y distributions are supplemented by an extended distribution, which contains $(1 - C_X)$ 20% of the Zr and 40% of the Y.

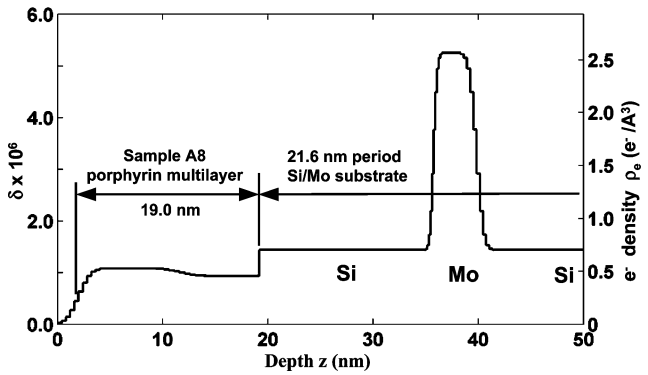

Figure 6. Model for the electron density profile (shown also as the index of refraction parameter, δ) that was used for the fit in Figure 5d. Only the topmost Si/Mo bilayer is shown.

possible model for the film, namely, a single-slab model, a resonant cavity effect was predicted but resulted in a poor fit to the observed reflectivity. After various trials, the more complex model shown in Figure 6, which has a slight buildup of electron density in the top half of the film, was found to yield a reasonable simulation of the reflectivity and was subsequently found to give very reasonable fits for the X-ray fluorescent yields. In our computational scheme, the **E** field intensity, $I(\theta,z)$, is a function of the incident angle (θ) and position (z) above the substrate surface. $I(\theta,z)$ is computed once, stored in a data file, and then used to calculate the fluorescence yield according to the formula $Y(\theta) = \int \rho(z)\, I(\theta,z)\, dz$ for various models of the unknown atomic distribution of the metal atom layers. Figure 7 shows the **E** field intensity as a surface in $\theta-z$ space. The first and second modes of the resonant cavity effect (indicated with arrows) show a normalized **E** field intensity value in excess of 4, which

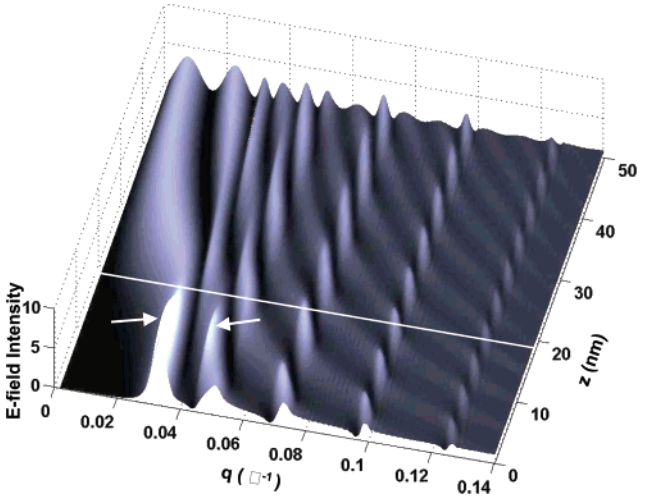

Figure 7. Surface plot of the calculated **E** field intensity as a function of the scattering vector, q, and position, z, above the substrate surface for sample A8. The white line indicates the film/air interface of the sample. The arrows indicate the first two modes of a resonant cavity or waveguide effect in the sample film that gives rise to the dip in the XRR (Figure 5d) and large-yield peaks (Figures 5a−c) at the same value of q.

is the maximum value in the vacuum region above the film. At higher angles, the effect of the film on the **E** field intensity dramatically diminishes and can be ignored.

The X-ray fluorescent yield data and simulations for Zr Kα, Y Kα, and Hf Lα of sample A8 are shown in Figure 5a−c. XRF coverage measurement results are shown in Table 1. All the data shown in Figure 5 were collected simultaneously. Note that each element has a distinct fluorescence yield curve, with the most pronounced differences occurring in the first two Bragg peaks.

Referring to the schematic diagram of sample A8 shown in Figure 1, we expected Zr and Y to occupy thin layers at the bottom and top of the film, respectively, while Hf would be found throughout the film, except at the very bottom and top. From Figure 7 we see that the first mode of the resonant cavity will strongly affect all atoms inside the film while atoms at the top of the film will show no affect, since the resonance creates an **E** field intensity node at the film−air interface. X-ray fluorescence peaks coinciding with the position of the dip in the reflectivity data for all three elements are clearly visible, indicating that Zr, Hf, and Y are present inside the film. Figure 5 also shows simulations of X-ray fluorescence yields. For the Zr Kα fluorescence yield (Figure 5a), the Zr distribution, $\rho(z)$, was partitioned into two parts: (1) a fraction C_{Zr} of the total Zr contained within a Gaussian and (2) the remainder $(1 - C_{Zr})$ of Zr atoms contained in precipitate particles possibly from incompletely dissolved ZrOCl salt. These latter Zr atoms are modeled by an extended uniform distribution from $z = 0$ to $z = 219$ nm, the upper limit being chosen to be several times larger than the longest XSW period generated by the LSM at the low q end of the scan range. The best fit for this model has $C_{Zr} = 0.8$ with the Zr Gaussian distribution centered at $z = 0.8$ nm from the top of the substrate surface and having a width of $\sigma = 0.4$ nm. The Hf Lα XSW yield (Figure 5c) was best fit by a model that used a uniform slab from $z = 1.0$ nm to $z = 18.0$ nm, which bounds the expected Hf position on the basis of Figure 1. Hf coverage modeled by an extended uniform distribution did not improve the fit to the data. The XSW-determined Zr and Hf distributions are in very reasonable agreement with the model for film A8 depicted in Figure 1. However, Y, which was intended to serve as

a marker atom for the terminal phosphonate position, failed to do so and apparently diffused inward uniformly throughout the film. The best simple model for Y Kα fluorescence was found to be a rectangle profile uniformly distributed throughout the film plus an extended uniform distribution with $C_Y = 0.6$, where C_Y is the fraction contained in the rectangular profile. Apparently, *Y* did not selectively bind to the terminal phosphonate positions of the eighth porphyrin layer as desired, but instead was able to diffuse into the film and bind at other locations. XRF measurements support the XSW finding with the *Y* coverage was measured to be 14.0 nm^{-2}, well in excess of the coverage of ~1.3 or ~3.1 nm^{-2} that was found for the single layers of Zr and Hf, respectively.

In Figure 5 we also present some alternate model simulations as a comparison to the best-fit simulations. Figure 5b shows the fluorescence yield resulting from the expected position for Y, which was modeled to be a Gaussian distribution centered at $z = 18.5$ nm from the top of the substrate surface and having a width of $\sigma = 0.4$ nm. We see that the predicted Y fluorescence yield is unique and complex, proving that Y certainly is not confined to the expected terminal location. Further studies, to be published elsewhere, have found such dramatic modulations when successfully using Hf to mark the terminal phosphonate position instead of Y. Figure 5c shows the yield simulation that would result for $C_{Hf} = 0$ (100% of the Hf contained in an extended uniform distribution). We see that, for Hf, the extended uniform distribution model does not simulate the observed fluorescence at low angle but does so reasonably well for the third- and fourth-order Bragg reflections. Referring to Figure 7, we see that atoms distributed uniformly throughout the film will overlap nearly a whole period of the XSW for the third Bragg reflection and nearly two whole periods for the fourth Bragg reflection. The Hf distribution in sample A8 appears to be uniformly distributed when examined by the third- and fourth-order Bragg XSW yields and is thus modeled equivalently by both the slab shown in the inset in Figure 7c and the much larger slab used for the extended uniform distribution model. The true nature of the Hf distribution only becomes known by examining the fluorescence yield from the longer period XSW generated by the first- and second-order Bragg reflections. This illustrates why it is useful to examine the atomic distributions with several different XSW periods to appropriately match the length scale of the unknown atomic distribution.

Sample A1 uses a complex molecule with rotational freedom of the constituent porphyrins about the Re−Re axes, which form the sides of the "porphyrin square". (See Figure 2.) We consider two limiting conformations of the porphyrin-square molecule. In conformation A, the porphyrin PO_3-PO_3 axes are perpendicular to the plane of the square, and in conformation B, the porphyrin constituents rotate about the Re−Re axes and lie approximately flat in the plane of the square. (Note, however, that a *completely* flat conformation is sterically prohibited.) For conformation A, the formation of a monolayer takes the place of the four PO_3 positions on one side of the square to the Zr-terminated surface, with the PO_3-PO_3 axes standing normal to the surface. In the capping step, Y atoms bind to the terminal PO_3 positions. In this configuration, if we assign Zr to be located at z_0, the Zn/Re would be at $z_0 + 1.25$ nm and Y at $z_0 + 2.5$ nm. For conformation B, all heavy atoms would be approximately at the same location. Data from sample D8, which is based on the same molecule, suggest an average layer thickness of 13.0/8 = 1.63 nm/layer. For comparison, AFM measurements of

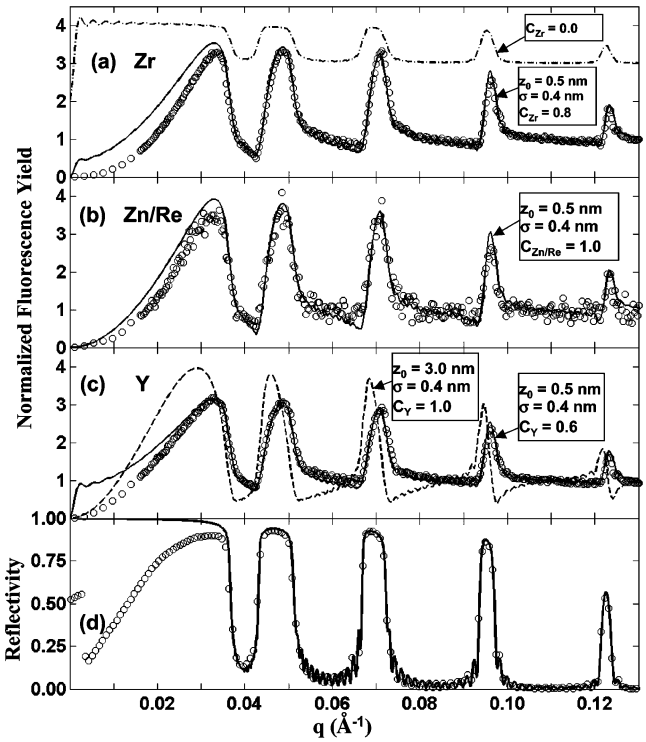

Figure 8. Sample A1 XSW results. (a−c) Simultaneously measured X-ray fluorescence yields for Zr Kα, Zn Kα + Re Lα, and Y Kα (open circles) and best theoretical fits (solid lines). A theoretical simulation for Y (dashed line) using a Gaussian model for Y centered at $z = 3.0$ nm is shown in (c). A theoretical simulation (dashed−dotted line offset vertically by 2 for clarity) in (a) is shown for a 100% extended uniform distribution model. (d) Measured (open circles) and theoretical fit (solid line) of X-ray reflectivity.

square films yield (with somewhat less precision and on inherently rougher surfaces) an average layer thickness of ca. 1.9 nm, i.e., in good agreement with the X-ray result.[25] Comparing 1.63 nm/layer with 2.5 nm/layer for a square having the limiting perpendicular conformation, A, an average porphyrin wall angle of 40°, roughly midway between the two limiting conformations, is implied.

XSW results of sample A1 are presented in Figure 8. In parts a−c of Figure 8 we first show the measured X-ray fluorescence yields for Zr Kα, Zn Kα + Re Lα, and Y Kα, respectively. (The Zn K and Re L peaks were inseparable due to overlap in the fluorescence spectra. However, this is not overly detrimental to the analysis, since Zn and Re atoms are expected to be located at the same height as illustrated in Figure 2.) The three elements show very similar distributions. In Figure 8a, the Zr distribution is modeled with a Gaussian profile, $C_{Zr} = 0.8$, centered at 0.5 nm with $\sigma = 0.4$ nm. In Figure 8b, the Zn/Re distribution is modeled in a Gaussian profile, $C_{Zn/Re} = 1.0$, centered at 0.5 nm with $\sigma = 0.4$ nm. In Figure 8c, the Y distribution is modeled in a Gaussian profile, $C_Y = 0.6$, centered at 0.5 nm with $\sigma = 0.4$ nm. We see that Zr, Zn/Re, and Y are all well modeled by very narrow distributions centered at $z = 0.5$ nm from the substrate surface. It is very interesting that Zr and Y, which were delivered from aqueous solutions, require considerable fractions to be modeled by extended uniform distributions, while the Zn/Re pair was best fit by assuming 100% in the surface layer modeled by a Gaussian distribution. This suggests that the porphyrin-square molecule dispersed well and had no tendency to agglomerate or otherwise crystallize into nonmonolayer conformations. For comparison, Figure 8c shows the theoretical yield for Y if it had been in the

fully extended terminal phosphonate position at $z = 3$ nm. In addition, we show an extended uniform distribution in Figure 8a for comparison with the measured Zr yield. For this particular single-monolayer sample the XSW data strongly suggest that the one-layer porphyrin-square film of sample A1 is in a collapsed configuration. The previously discussed low Zn/Re coverage for A1 further substantiates this finding. This again demonstrates the strength of this combined XRF, XSW, and XRR approach.

Conclusions

In this study we demonstrated the use of the XSW technique with large-*d*-spacing LSMs for measuring 1-D atomic distribution profiles within nanometer-scale thin-film structures and applied this technique to the study of porphyrin-based metal/phosphonate multilayer films. We have shown that it is possible to distinguish between subnanometer slabs and distributions on the 20 nm length scale in the same sample. This was demonstrated by studying the Zr, Y, and Hf distributions in an eight-layer sample (A8). The XSW technique also allows the partitioning of atoms contained in the expected layer structure and those contained in extended uniform distributions due to random surface impurity particles that are not incorporated within the ultra-thin-film structure. Different types of atoms can be incorporated to simultaneously measure different features of the layer-by-layer nanoscale assembly.

The accuracy of our procedure for determining an atomic density profile, $\rho(z)$, from an XSW yield, $Y(q)$, relies on our accuracy in describing the **E** field intensity within the film. This requires an accurate modeling of the layers and interfaces with appropriate indices of refraction, which we verify by comparing the measured reflectivity with the model simulation. From this part of the analysis we found that the more conventional Debye−Waller factor treatment of the interface roughness and interdiffusion needed to be replaced by the more rigorous graded-interface model and that the Si/Mo and Mo/Si interfaces had different widths.

Zn (or Re) XRF coverage measurements of sample D8 showed a footprint of 12 nm^2 per porphyrin square, which is consistent with the lateral dimensions and expected packing of the molecules. Using XRR and XSW, we have clearly shown that the multilayer assembly process proceeds as expected when the spacer molecule is a simple porphyrin but deviates substantially from expectation when the complex macromolecular porphyrin square is used. The preliminary conclusion is that the first layer of the porphyrin-square multilayer adopts a collapsed conformation on the surface to yield a measured thickness well below the expected 2.1 nm. Subsequent layers of the porphyrin-square multilayer film are more "regular" in density, but the smaller-than-expected thickness indicates a tilt away from the vertical orientation. These observations are supported by independent AFM studies[25] where the idealized structure shown in Figure 1 is not observed for the first layer and moderate tilting exists in the subsequent layer. Consequently, our films can be envisioned as having a semiordered structure that becomes more regular and ordered after the first few layers, which serve as the foundation for the overall film structure. That a high metal coverage is observed for our porphyrin-square multilayer films may result from an additional metal incorporation into the nanoporous structure of the films and not at the phosphonate sites. Whereas Y did not selectively occupy the terminal phosphonate position as expected, we found that Hf is a more suitable choice as a marker atom for the top layer, and this will be used in future studies.

We were able to simultaneously differentiate very narrow monolayer slabs and rather large slabs (∼17 nm) because the multiple Bragg peaks produced XSWs with periods spanning all the length scales concerned. Despite the fact that the eight-layer-thick film of sample A8 poses a complex coupled problem for XRR and XSW, a relatively simple model that did not assume the Zr, Hf, and Y profiles was successful in predicting the observed fluorescence yields.

Acknowledgment. We thank D. Goodner, J. Carsello, and Z. Zhong for technical support. This work was supported by the National Science Foundation (NSF) under Contract No. EEC-0118025 to the Nanoscale Science and Engineering Center at Northwestern University (NU), the Department of Energy (DOE) under Contract No. DE-FG02-03ER15457 to the Institute for Environmental Catalysis at NU, the Camille and Henry Dreyfus Post-doctoral Program in Environmental Chemistry (fellowship for R.W.G.), the National Institutes of Health (Contract No. GM62109-02), the NU Institute for Bioengineering and Nanoscience in Advanced Medicine, and the DOE (Contract No. DE-FG02-01ER15244). This work made use of the NSLS facilities at the Brookhaven National Laboratory supported by the DOE (Grant DE-AC02-98CH10886), the NU Central Facilities supported by the MRSEC program of the NSF (Grant DMR-0076097), and the APS X-ray Optics Fabrication Facilities at Argonne National Laboratory supported by the DOE-BES (Grant W-31-109-Eng-38).

LA048904B